

# Neutrino Interactions at Ultrahigh Energies

Raj Gandhi\*

*Mehta Research Institute  
Chhatnag Road, Jhusi, Allahabad 211019, India*

Chris Quigg†

*Theoretical Physics Department, Fermi National Accelerator Laboratory  
P.O. Box 500, Batavia, Illinois 60510 USA*

Mary Hall Reno‡

*Department of Physics and Astronomy, University of Iowa  
Iowa City, Iowa 52242 USA*

Ina Sarcevic§

*Department of Physics, University of Arizona  
Tucson, Arizona 85721 USA  
(November 26, 2024)*

## Abstract

We report new calculations of the cross sections for deeply inelastic neutrino-nucleon scattering at neutrino energies between  $10^9$  eV and  $10^{21}$  eV. We compare with results in the literature and assess the reliability of our predictions. For completeness, we briefly review the cross sections for neutrino interactions with atomic electrons, emphasizing the role of the  $W$ -boson resonance in  $\bar{\nu}_e e$  interactions for neutrino energies in the neighborhood of 6.3 PeV. Adopting model predictions for extraterrestrial neutrino fluxes from active galactic nuclei, gamma-ray bursters, and the collapse of topological defects, we estimate

---

\*E-mail: raj@mri.ernet.in

†E-mail: quigg@fnal.gov

‡E-mail: reno@hepsun1.physics.uiowa.edu

§E-mail: ina@gluon.physics.arizona.edu

event rates in large-volume water Čerenkov detectors and large-area ground arrays.

## I. INTRODUCTION

Neutrino observatories hold great promise for probing the deepest reaches of stars and galaxies [1–4]. Unlike charged particles, neutrinos arrive on a direct line from their source, undeflected by magnetic fields. Unlike photons, neutrinos interact weakly, so they can penetrate thick columns of matter. For example, the interaction length of a 1-TeV neutrino is about 2.5 million kilometers of water, or 250 kilotonnes/cm<sup>2</sup>, whereas high-energy photons are blocked by a few hundred grams/cm<sup>2</sup>.

Ultrahigh-energy neutrinos can be detected by observing long-range muons produced in charged-current neutrino-nucleon interactions. To reduce the background from muons produced in the atmosphere, it is advantageous to site a neutrino telescope at a depth of several kilometers (water equivalent) or to observe upward-going muons. The reactions  $(\nu_\ell, \bar{\nu}_\ell)N \rightarrow (\ell^-, \ell^+) + \text{anything}$  and  $(\nu_\ell, \bar{\nu}_\ell)N \rightarrow (\nu_\ell, \bar{\nu}_\ell) + \text{anything}$  are the major sources of both the desired signal and the attenuation of the neutrino “beam” as it passes through the Earth *en route* to the detector. Through the past dozen years, improving knowledge of the partonic structure of the nucleon has made possible a series of increasingly refined predictions for the interaction cross sections [5–13]. Over the same period, ideas about the flux of neutrinos from active galactic nuclei (AGNs) and other extraterrestrial sources have evolved considerably. The observation [14] of neutrinos correlated with supernova SN1987A and the detection of solar neutrinos by observing the direction of recoil electrons from neutrino interactions [15,16] showed the promise of neutrino observatories for astrophysical studies. The detection of neutrinos produced by cosmic-ray interactions in the Earth’s atmosphere [17–20] has emerged as a tool for investigating neutrino oscillations [21–24]. Plans for neutrino observatories that will detect neutrinos that originate beyond Earth have matured to the point that it is now reasonable to contemplate instrumenting a volume of water or ice as large as 1 km<sup>3</sup>. [25–32]. The ground array of the proposed Pierre Auger Cosmic Ray Observatory [33] would have an acceptance exceeding 1 km<sup>3</sup> sr of water for neutrino energies greater than 10<sup>17</sup> eV [34]. The Orbiting Wide-angle Light collectors project (OWL) would place in Earth orbit a lens to study air showers initiated by > 10<sup>20</sup>-eV particles, including neutrinos [35].

In this paper we present new calculations of the cross sections for charged-current and neutral current interactions of neutrinos with nucleons, updating our results of Ref. [12] (GQRS96) to take account of new information about the parton distributions within the nucleon [36]. In place of the CTEQ3–DIS parton distributions [37] that we adopted as our nominal set in GQRS96, we base our new calculations on the CTEQ4–DIS parton distributions [38]. The changes are modest, and only noticeable at the highest neutrino energies we consider: at  $E_\nu = 10^{21}$  eV, the new cross sections are about 25% smaller than those of GQRS96. We find that for neutrino energies up to 10<sup>16</sup> eV, all the standard sets of parton distribution functions yield very similar cross sections. At higher energies, the predictions rely on incompletely tested assumptions about the behavior of parton distributions at very small values of the momentum fraction  $x$ . The resulting uncertainty reaches a factor 2<sup>±1</sup> around 10<sup>20</sup> eV.

We combine our new evaluations of the neutrino-nucleon cross sections with models for the flux of ultrahigh-energy (UHE) neutrinos to estimate event rates in neutrino observatories. We consider the diffuse flux of neutrinos from AGNs and the flux of neutrinos that

may accompany gamma-ray bursts, as well as neutrinos from cosmological sources such as the decay of topological defects formed in the early universe. We evaluate rates for upward-going muons produced in or beneath large underwater and ice detectors, and we compute rates for contained neutrino interactions in a  $\text{km}^3$  volume. We have also estimated rates for the proposed ground array of the Pierre Auger Cosmic Ray Observatory.

The detection of upward-going muons from AGNs looks feasible in the next generation of underground experiments with effective areas on the order of  $0.1 \text{ km}^2$ . As the muon energy threshold increases above a few TeV, atmospheric neutrinos and muons become less important backgrounds. Downward and air-shower event rates look promising for  $\text{km}^3$  detectors, for a variety of models.

In the next Section, we review the calculation of the neutrino-nucleon charged-current and neutral-current cross sections, their sensitivities to parton distribution functions, and the resulting neutrino-nucleon interaction lengths. We also give a brief account of neutrino-electron cross sections and interaction lengths. Ultrahigh-energy neutrino rates for a selection of flux models appear in §III. Our summary and conclusions make up §IV.

## II. NEUTRINO-NUCLEON INTERACTIONS

### A. Inclusive cross sections

We calculate the inclusive cross section for the reaction

$$\nu_\mu N \rightarrow \mu^- + \text{anything}, \quad (2.1)$$

where  $N \equiv \frac{n+p}{2}$  is an isoscalar nucleon, in the renormalization group-improved parton model. The differential cross section is written in terms of the Bjorken scaling variables  $x = Q^2/2M\nu$  and  $y = \nu/E_\nu$  as

$$\frac{d^2\sigma}{dx dy} = \frac{2G_F^2 M E_\nu}{\pi} \left( \frac{M_W^2}{Q^2 + M_W^2} \right)^2 \left[ xq(x, Q^2) + x\bar{q}(x, Q^2)(1-y)^2 \right], \quad (2.2)$$

where  $-Q^2$  is the invariant momentum transfer between the incident neutrino and outgoing muon,  $\nu = E_\nu - E_\mu$  is the energy loss in the lab (target) frame,  $M$  and  $M_W$  are the nucleon and intermediate-boson masses, and  $G_F = 1.16632 \times 10^{-5} \text{ GeV}^{-2}$  is the Fermi constant. The quark distribution functions are

$$q(x, Q^2) = \frac{u_v(x, Q^2) + d_v(x, Q^2)}{2} + \frac{u_s(x, Q^2) + d_s(x, Q^2)}{2} + s_s(x, Q^2) + b_s(x, Q^2) \quad (2.3)$$

$$\bar{q}(x, Q^2) = \frac{u_s(x, Q^2) + d_s(x, Q^2)}{2} + c_s(x, Q^2) + t_s(x, Q^2),$$

where the subscripts  $v$  and  $s$  label valence and sea contributions, and  $u, d, c, s, t, b$  denote the distributions for various quark flavors in a *proton*. At the energies of interest for neutrino

astronomy, perturbative QCD corrections to the cross section formula (2.2) are insignificant. In the DIS factorization scheme appropriate to the CTEQ4–DIS parton distributions, the terms proportional to  $\alpha_s$  [39] in the NLO cross section contribute only a few percent, so we omit them.

The  $t\bar{t}$  sea is a negligible component of the nucleon over the  $Q^2$ -range relevant to neutrino-nucleon scattering; accordingly we neglect it. At the energies of interest here, it is a sound kinematical simplification to treat charm and bottom quarks as massless. However, the threshold suppression of the  $b \rightarrow t$  transition must be taken into account. We adopt the standard “slow-rescaling” prescription [40], with  $m_t = 175 \text{ GeV}/c^2$ . We have carried out numerical integrations using the adaptive Monte Carlo routine VEGAS [41], and Gaussian techniques.

The neutral-current cross section is of interest because it contributes to the attenuation of neutrinos as they pass through the Earth. Neutral-current  $\nu N$  interactions may also be significant backgrounds to the observation of the resonant formation process  $\bar{\nu}_e \rightarrow W^-$ . If it becomes possible to measure neutral-current reactions and characterize the neutrino energy, Carena, *et al.* [42] have shown that the neutral-current to charged-current ratio is an important discriminant of new physics.

Within the electroweak theory, a calculation parallel to the one described above leads to the neutral-current cross section. The differential cross section for the reaction  $\nu_\mu N \rightarrow \nu_\mu + \text{anything}$  is given by

$$\frac{d^2\sigma}{dx dy} = \frac{G_F^2 M E_\nu}{2\pi} \left( \frac{M_Z^2}{Q^2 + M_Z^2} \right)^2 \left[ xq^0(x, Q^2) + x\bar{q}^0(x, Q^2)(1-y)^2 \right], \quad (2.4)$$

where  $M_Z$  is the mass of the neutral intermediate boson. The quantities involving parton distribution functions are

$$\begin{aligned} q^0(x, Q^2) &= \left[ \frac{u_v(x, Q^2) + d_v(x, Q^2)}{2} + \frac{u_s(x, Q^2) + d_s(x, Q^2)}{2} \right] (L_u^2 + L_d^2) \\ &+ \left[ \frac{u_s(x, Q^2) + d_s(x, Q^2)}{2} \right] (R_u^2 + R_d^2) + \\ &[s_s(x, Q^2) + b_s(x, Q^2)](L_d^2 + R_d^2) + [c_s(x, Q^2) + t_s(x, Q^2)](L_u^2 + R_u^2) \end{aligned} \quad (2.5)$$

$$\begin{aligned} \bar{q}^0(x, Q^2) &= \left[ \frac{u_v(x, Q^2) + d_v(x, Q^2)}{2} + \frac{u_s(x, Q^2) + d_s(x, Q^2)}{2} \right] (R_u^2 + R_d^2) \\ &+ \left[ \frac{u_s(x, Q^2) + d_s(x, Q^2)}{2} \right] (L_u^2 + L_d^2) + \\ &[s_s(x, Q^2) + b_s(x, Q^2)](L_d^2 + R_d^2) + [c_s(x, Q^2) + t_s(x, Q^2)](L_u^2 + R_u^2), \end{aligned} \quad (2.6)$$

where the chiral couplings are

$$\begin{aligned} L_u &= 1 - \frac{4}{3}x_W & L_d &= -1 + \frac{2}{3}x_W \\ R_u &= -\frac{4}{3}x_W & R_d &= \frac{2}{3}x_W \end{aligned} \quad (2.7)$$

and  $x_W = \sin^2 \theta_W$  is the weak mixing parameter. For numerical calculations we have chosen  $x_W = 0.226$ , consistent with recent measurements [43]. Again the top-quark sea is negligible.

We show the cross section for the charged-current reaction  $\nu_\mu N \rightarrow \mu^- + \text{anything}$  as a function of the neutrino energy  $E_\nu$  in Figure 1 (thin solid line). At low energies the charged-current cross section  $\sigma_{\text{CC}}$  rises linearly with  $E_\nu$ . For energies exceeding about  $10^4$  GeV, the cross section is damped by the  $W$ -boson propagator. We also show in Figure 1 the neutral-current cross section  $\sigma_{\text{NC}}$  for the reaction  $\nu_\mu N \rightarrow \nu_\mu + \text{anything}$  (dashed line), together with  $\sigma_{\text{tot}}$ , the sum of charged-current and neutral-current cross sections (thick solid line). For the range of neutrino energies of interest here, the charged-current results apply equally to the reaction  $\nu_e N \rightarrow e^- + \text{anything}$ . The neutral-current cross section for the reaction  $\nu_e N \rightarrow \nu_e + \text{anything}$  is identical to  $\sigma_{\text{NC}}$  depicted here.

The CTEQ4–DIS parton distributions are somewhat less singular as  $x \rightarrow 0$  than the CTEQ3–DIS parton distributions we adopted as our nominal set in GQRS96. Specifically, the sea-quark distributions of the CTEQ4 set behave as

$$xq_s^{[\text{CTEQ4}]}(x) \propto x^{-0.227} \quad (2.8)$$

near  $x = 0$ , whereas those of the CTEQ3 set behave as

$$xq_s^{[\text{CTEQ3}]}(x) \propto x^{-0.332} . \quad (2.9)$$

The gentler singularity of the CTEQ4 distributions implies a smaller cross section at the highest energies, where the predominant contributions to the cross section come from very small values of  $x$ . We show in Figure 2 the ratio of the charged-current cross sections calculated using the CTEQ4–DIS and CTEQ3–DIS parton distributions. Up to  $E_\nu \approx 10^7$  GeV, the two evaluations agree within a few percent. At still higher energies, the CTEQ4 cross section falls below the CTEQ3 cross section. At the highest energy we consider,  $E_\nu = 10^{12}$  GeV, the ratio is 0.74. This is a small change.

Similar calculations lead to the cross sections for  $\bar{\nu}N$  scattering. We show in Figure 3 the neutral-current (dashed line), charged-current (thin solid line), and total (thick solid line)  $\bar{\nu}N$  cross sections. At low energies, where the contributions of valence quarks predominate, the  $\bar{\nu}N$  cross sections are smaller than the corresponding  $\nu N$  cross sections, because of the familiar  $(1-y)^2$  behavior of the  $\bar{\nu}q$  cross sections. Above  $E_\nu \approx 10^6$  GeV, the valence contribution is negligible and the  $\nu N$  and  $\bar{\nu}N$  cross sections become equal.

We collect in Tables I and II the charged-current, neutral-current, and total cross sections for  $\nu N$  and  $\bar{\nu}N$  interactions, respectively. For the angular distributions, characterized by the mean inelasticity parameter  $\langle y \rangle$ , we refer to the CTEQ3 values we presented in Tables 1 and 2 of Ref. [12].

For  $10^{16}$  eV  $\leq E_\nu \leq 10^{21}$  eV, the CTEQ4–DIS cross sections are given within 10% by

$$\begin{aligned} \sigma_{\text{CC}}(\nu N) &= 5.53 \times 10^{-36} \text{ cm}^2 \left( \frac{E_\nu}{1 \text{ GeV}} \right)^{0.363} \\ \sigma_{\text{NC}}(\nu N) &= 2.31 \times 10^{-36} \text{ cm}^2 \left( \frac{E_\nu}{1 \text{ GeV}} \right)^{0.363} \\ \sigma_{\text{tot}}(\nu N) &= 7.84 \times 10^{-36} \text{ cm}^2 \left( \frac{E_\nu}{1 \text{ GeV}} \right)^{0.363} \end{aligned}$$

$$\sigma_{\text{CC}}(\bar{\nu}N) = 5.52 \times 10^{-36} \text{ cm}^2 \left( \frac{E_\nu}{1 \text{ GeV}} \right)^{0.363} \quad (2.10)$$

$$\sigma_{\text{NC}}(\bar{\nu}N) = 2.29 \times 10^{-36} \text{ cm}^2 \left( \frac{E_\nu}{1 \text{ GeV}} \right)^{0.363}$$

$$\sigma_{\text{tot}}(\bar{\nu}N) = 7.80 \times 10^{-36} \text{ cm}^2 \left( \frac{E_\nu}{1 \text{ GeV}} \right)^{0.363}.$$

## B. Variant parton distributions

The CDF Collaborations's suggestion [44] that the yield of jets in the reaction  $\bar{p}p \rightarrow \text{jet}_1 + \text{jet}_2 + \text{anything}$  exceeds the rate expected in standard quantum chromodynamics has prompted a re-examination of the uncertainties of parton distributions at moderate and large values of  $x$ . In particular, the CTEQ Collaboration has produced a variant of the CTEQ4 distributions, labelled CTEQ4–HJ, in which an enhanced gluon population at large values of  $x$  raises the predicted two-jet inclusive cross section. The increased gluon density at large  $x$  can affect the small- $x$  sea-quark distributions at large values of  $Q^2$ , so it is interesting to ask what difference the variant parton distributions would make for the UHE neutrino cross sections.

We show in Figure 4 the UHE  $\nu N$  cross sections calculated with the CTEQ4–HJ parton distributions. They are quite similar to those calculated with the standard CTEQ4–DIS distributions. The ratio of CTEQ4–HJ to CTEQ4–DIS cross sections is displayed in Figure 5. The difference is less than 5% up to  $10^8$  GeV, and is smaller than 15% at the highest energy we consider. It is of no consequence for neutrino observatories.

## C. Assessment

How well is it possible to predict  $\sigma(\nu_\ell N \rightarrow \ell + \text{anything})$  and  $\sigma(\nu_\ell N \rightarrow \nu_\ell + \text{anything})$ ? For  $E_\nu \lesssim 10^{16}$  eV, all the standard sets of parton distributions, by which we mean those fitted to a vast universe of data, yield very similar cross sections [12,13,10,11], within the standard electroweak theory. For  $E_\nu \gtrsim 10^{16}$  eV, cross sections are sensitive to the behavior of parton distributions at very small  $x$ , where there are no direct experimental constraints. At these high energies, different *assumptions* about  $x \rightarrow 0$  behavior then lead to different cross sections. Judging from the most extreme variations we found in GQRS96, and from our present calculations, we conclude that at  $10^{20}$  eV, the uncertainty reaches a factor of  $2^{\pm 1}$ .

New physics can, of course, modify the UHE cross sections. The contributions of superpartners have been evaluated by Carena, *et al.* [42]. Doncheski and Robinett [45] have investigated leptoquark excitation. Bordes and collaborators [46] have speculated that new interactions might dramatically increase the UHE  $\nu N$  cross sections, but Burdman, Halzen, and Gandhi have countered [47] that unitarity limits the growth of the UHE cross section.

## D. Interaction lengths

The neutrino beams produced in accelerator laboratories are purified by passage through several kilometers (water equivalent) of material, which absorbs any accompanying particles without attenuating the neutrino flux. The story is different at the ultrahigh energies of interest to neutrino astronomy. The rise of the charged-current and neutral-current cross sections with energy is mirrored in the decrease of the (water-equivalent) interaction length,

$$\mathcal{L}_{\text{int}} = \frac{1}{\sigma_{\nu N}(E_\nu)N_A}, \quad (2.11)$$

where  $N_A = 6.022 \times 10^{23} \text{ mol}^{-1} = 6.022 \times 10^{23} \text{ cm}^{-3}$  (water equivalent) is Avogadro's number. The energy dependence of the interaction lengths for neutrinos on nucleons is shown in Figure 6. We show separately the interaction lengths for charged-current and neutral-current reactions, as well as the interaction length corresponding to the total (charged-current plus neutral-current) cross section. The same information is shown for antineutrinos on nucleons in Figure 7. Above about  $10^{16}$  eV, the two sets of interaction lengths coincide. These results apply equally to  $\nu_e N$  (or  $\bar{\nu}_e N$ ) collisions as to  $\nu_\mu N$  (or  $\bar{\nu}_\mu N$ ) collisions.

Over the energy range of interest for neutrino astronomy, the interactions of  $\nu_e$ ,  $\nu_\mu$ , and  $\bar{\nu}_\mu$  with electrons in the Earth can generally be neglected in comparison to interactions with nucleons. The case of  $\bar{\nu}_e e$  interactions is exceptional, because of the intermediate-boson resonance formed in the neighborhood of  $E_\nu^{\text{res}} = M_W^2/2m \approx 6.3 \times 10^{15}$  eV. The resonant reactions  $\bar{\nu}_e e \rightarrow W^- \rightarrow \bar{\nu}_\mu \mu$  and  $\bar{\nu}_e e \rightarrow W^- \rightarrow \text{hadrons}$  may offer a detectable signal. At resonance, the reaction  $\bar{\nu}_e e \rightarrow W^- \rightarrow \text{anything}$  significantly attenuates a  $\bar{\nu}_e$  beam propagating through the Earth. The water-equivalent interaction lengths corresponding to the neutrino-electron cross sections computed in [12] are displayed in Figure 8. These are evaluated as

$$\mathcal{L}_{\text{int}}^{(e)} = \frac{1}{\sigma_{\nu e}(E_\nu)(10/18)N_A}, \quad (2.12)$$

where  $(10/18)N_A$  is the number of electrons in a mole of water.

We have reviewed current knowledge of the structure of the Earth in Ref. [12]. To good approximation, the Earth may be regarded as a spherically symmetric ball with a complex internal structure consisting of a dense inner and outer core and a lower mantle of medium density, covered by a transition zone, lid, crust, and oceans. A neutrino emerging from the nadir has traversed a column whose depth is 11 kilotonnes/cm<sup>2</sup>, or  $1.1 \times 10^{10}$  cmwe. The Earth's diameter exceeds the charged-current interaction length of neutrinos with energy greater than 40 TeV. In the interval  $2 \times 10^6 \text{ GeV} \lesssim E_\nu \lesssim 2 \times 10^7 \text{ GeV}$ , resonant  $\bar{\nu}_e e$  scattering adds dramatically to the attenuation of electron antineutrinos. At resonance, the interaction length due to the reaction  $\bar{\nu}_e e \rightarrow W^- \rightarrow \text{anything}$  is 6 tonnes/cm<sup>2</sup>, or  $6 \times 10^6$  cmwe, or 60 kmwe. The resonance is effectively extinguished for neutrinos that traverse the Earth. In the estimates of event rates that follow in §III, we take account of the effect of attenuation on upward-going neutrinos.



### III. ASTROPHYSICAL NEUTRINO FLUXES: UHE EVENT RATES

Since the publication of the GQRS96 cross sections and event rates [12], several new models of the diffuse neutrino flux from active galactic nuclei (AGNs) have appeared [48,49]. In addition, Waxman and Bahcall [50] have argued that it might be possible to detect neutrinos associated with gamma-ray bursts. New models have also been put forward for the production of neutrinos in the decays of generic heavy particles [51] and in the collapse of topological defects [52].

It is therefore timely to reconsider the event rates to be expected in large-volume detectors. We focus on the production of upward-going muons in the charged-current reactions  $(\nu_\mu, \bar{\nu}_\mu)N \rightarrow (\mu^-, \mu^+) + \text{anything}$ . Upward-going muons are free of background from the flux of muons produced by cosmic-ray interactions in the atmosphere. It is in any case advantageous to site a detector beneath several kmwe to shield it from the (downward) rain of atmospheric muons [53]. Even at 3 kmwe underground, a detector still sees more than 200 vertical muons  $\text{km}^{-2} \text{s}^{-1} \text{sr}^{-1}$ , though most of these muons are quite soft. If we impose the requirement that  $E_\mu^{\text{min}} > (10^3, 10^4, 10^5) \text{ GeV}$ , the flux is  $(7, 3 \times 10^{-2}, 6 \times 10^{-5}) \text{ muons km}^{-2} \text{s}^{-1} \text{sr}^{-1}$  [54]. As the incident zenith angle of the atmospheric muons increases, the background flux decreases. For horizontal incidence and below, the muon rate observed underground should be largely background-free. There is another important reason for looking down: The few-km range of UHE muons means that large-volume detectors can observe charged-current events that occur not only within the instrumented volume, but also in the rock or water underlying the detector. Accordingly, the effective volume of a detector may be considerably larger than the instrumented volume, for upward-going muons. For energies above 40 TeV, the Earth's diameter exceeds the interaction length of neutrinos. At these energies it is beneficial to look for events induced by downward and horizontal neutrino conversions to muons [57].

#### A. Sources of UHE Neutrinos

We display in Figure 9 the neutrino fluxes calculated in a number of models. Neutrinos produced by cosmic-ray interactions in Earth's atmosphere dominate over other neutrino sources at energies below a few TeV. In this energy régime, the flux of atmospheric neutrinos is derived from the decay of charged pions and kaons. The dotted curve in Figure 9 shows the angle-averaged atmospheric (ATM)  $\nu_\mu + \bar{\nu}_\mu$  flux calculated by Volkova [58,59], which we parametrize as

$$\frac{dN_{\nu_\mu + \bar{\nu}_\mu}}{dE_\nu} = 7.8 \times 10^{-11} \left( \frac{E_\nu}{1 \text{ TeV}} \right)^{-3.6} \text{ cm}^{-2} \text{ s}^{-1} \text{ sr}^{-1} \text{ GeV}^{-1}. \quad (3.1)$$

The prompt neutrino flux from charm production in the atmosphere, a small additional component that appears above  $E_\nu \approx 1 \text{ TeV}$ , has been estimated recently by Pasquali, *et al.* [60].

Active galactic nuclei (AGNs) are the most powerful radiation sources in the universe, with luminosities on the order of  $10^{45 \pm 3} \text{ erg/s}$ . They are cosmic accelerators powered by the gravitational energy of matter falling in upon a supermassive black hole. Protons accelerated

to very high energies within an AGN may interact with matter in the accretion disk, or with ultraviolet photons in the bright jets along the rotation axis. Charged pions produced in the resulting  $pp$  or  $p\gamma$  collisions decay into muons and muon neutrinos. The subsequent muon decays yield additional muon neutrinos and electron neutrinos. Neutrino emission from AGNs may constitute the dominant diffuse flux at energies above a few TeV.

The solid lines in Figure 9 show the  $\nu_\mu + \bar{\nu}_\mu$  fluxes predicted in several contemporary models for neutrino production in AGNs: Protheroe’s model [48] of neutrinos produced in  $p\gamma$  interactions, denoted AGN-P96 ( $p\gamma$ ); and Mannheim’s model [49] of neutrino production in  $p\gamma$  interactions, denoted AGN-M95 ( $p\gamma$ ). The neutrino fluxes (AGN-SS91) [56] based on the pioneering work of Stecker and collaborators are still consistent with measurements. We retain the Stecker-Salamon flux considered in GQRS96 as a baseline to indicate the changes in event rates due to our new evaluation of the cross section.

A mechanism for gamma-ray bursts put forward by Waxman and Bahcall [50] also yields UHE neutrinos. The isotropic flux (GRB-WB) that results from a summation over sources is given by

$$\frac{dN_{\nu_\mu+\bar{\nu}_\mu}}{dE_\nu} = \mathcal{N} \left( \frac{E_\nu}{1 \text{ GeV}} \right)^{-n} \text{ cm}^{-2} \text{ s}^{-1} \text{ sr}^{-1} \text{ GeV}^{-1}, \quad (3.2)$$

with ( $\mathcal{N} = 4.0 \times 10^{-13}, n = 1$ ) for  $E_\nu < 10^5$  GeV, and ( $\mathcal{N} = 4.0 \times 10^{-8}, n = 2$ ) for  $E_\nu > 10^5$  GeV. Sigl, *et al.* [51] have explored a class of models of exotic heavy particle decays that ultimately lead to neutrinos in the final state. These are referred to as top-down (TD-SLSC) models. In particular, we consider the model in which the heavy  $X$ -particles have mass  $M_X = 2 \times 10^{16}$  GeV/ $c^2$ , which may arise from the collapse of networks of ordinary cosmic strings or from annihilations of magnetic monopoles. An interesting feature of this model is that the highest energy cosmic rays are photons. In the conventional topological defects model, the network of long strings loses its energy to the gravitation radiation. Wichoski, *et al.* [52] have proposed a model in which particle production is the dominant channel through which energy is lost. Even with the observational limits from Fréjus and Fly’s Eye as constraints, this non-scaling model (denoted TD-WMB) produces a much higher neutrino flux than the TD-SLSC model of Sigl, *et al.*, for the largest possible string mass density. The fluxes predicted by these exotic sources are shown as dashed curves in Figure 9.

The Super-Kamiokande Collaboration has recently presented evidence that muon neutrinos produced in the atmosphere oscillate into tau neutrinos or sterile neutrinos during their passage through the Earth [61]. At the neutrino energies of interest for the detection of extraterrestrial sources,  $E_\nu \gtrsim 1$  TeV, the probability for atmospheric neutrinos to oscillate *en route* to the detector,

$$P_{\nu_\mu \rightarrow \nu_x} \approx \sin^2 \left( 1.27 \times 10^{-6} \frac{\Delta m^2}{10^{-3} \text{ eV}^2} \cdot \frac{L}{1 \text{ km}} \cdot \frac{1 \text{ TeV}}{E_\nu} \right), \quad (3.3)$$

is less than  $10^{-3}$  for a path length  $L$  comparable to an Earth diameter ( $\approx 13,000$  km), if the neutrino mass-squared difference  $\Delta m^2 \approx 2.2 \times 10^{-3}$  eV $^2$ . For UHE neutrinos from distant sources, the oscillation probability may become interestingly large.

## B. Neutrino–nucleon interactions

The upward-muon event rate depends on the  $\nu_\mu N$  cross section in two ways: through the interaction length that governs the attenuation of the neutrino flux due to interactions in the Earth, and through the probability that the neutrino converts to a muon energetic enough to arrive at the detector with  $E_\mu$  larger than the threshold energy  $E_\mu^{\min}$ .

The probability that a muon produced in a charged-current interaction arrives in a detector with an energy above the muon energy threshold  $E_\mu^{\min}$  is given by

$$P_\mu(E_\nu, E_\mu^{\min}) = N_A \sigma_{CC}(E_\nu) \langle R(E_\nu; E_\mu^{\min}) \rangle, \quad (3.4)$$

where  $\langle R(E_\nu; E_\mu^{\min}) \rangle$  is the average range of a muon in rock [55] and  $N_A$  is Avogadro’s number. Although the Earth is transparent to low-energy neutrinos, an Earth diameter ( $1.1 \times 10^{10}$  cmwe) exceeds the interaction length of neutrinos with energies higher than about 40 TeV. For the isotropic fluxes presented in §III A, we represent the attenuation of neutrinos traversing the Earth by a shadow factor that is equivalent to the effective solid angle for upward muons, divided by  $2\pi$  [62]:

$$S(E_\nu) = \frac{1}{2\pi} \int_{-1}^0 d \cos \theta \int d\phi \exp[-z(\theta)/\mathcal{L}_{\text{int}}(E_\nu)]. \quad (3.5)$$

The column depth  $z(\theta)$  is plotted in Figure 15 of Ref. [12]. In our estimates of event rates, we choose the interaction length that corresponds to the total (charged-current plus neutral-current) cross section, which is shown for  $\nu_\mu N$  and  $\bar{\nu}_\mu N$  interactions as the solid curves in Figures 6 and 7. The shadow factor calculated using the CTEQ3–DIS parton distributions is shown in Figure 20 of Ref. [12].

The rate at which upward-going muons can be observed in a detector with effective area  $A$  is

$$\text{Rate} = A \int_{E_\mu^{\min}}^{E^{\max}} dE_\nu P_\mu(E_\nu; E_\mu^{\min}) S(E_\nu) \frac{dN}{dE_\nu}. \quad (3.6)$$

The integrals in (3.6) are evaluated up to  $E^{\max} = 10^{11}$  GeV except for AGN-SS91, for which the data files extend only to  $E^{\max} = 10^{9.8}$  GeV.

Let us consider for illustration a detector with effective area  $A = 0.1 \text{ km}^2$ . We show in Tables III and IV the annual event rates for upward-going muons with observed energies exceeding 1 TeV and 10 TeV, respectively. We tabulate rates for the full upward-going solid angle of  $2\pi$ , as well as for the detection of “nearly horizontal” muons with nadir angle  $\theta$  between  $60^\circ$  and  $90^\circ$ . The predicted event rates, shown here for the CTEQ4–DIS parton distributions, are very similar for other modern parton distributions.

The AGN fluxes introduced in §III A all yield significant rates for upward-going muon events, but the events induced by atmospheric neutrinos constitute an important background, especially for  $E_\mu^{\min} = 1 \text{ TeV}$ . The highest signal rates arise in the AGN-SS91 model. At the lower muon energy threshold,  $E_\mu^{\min} = 1 \text{ TeV}$ , this model yields rates about half the expected background from the interactions of atmospheric neutrinos. The expected background exceeds the signal rates for other models with the muon energy threshold set at

1 TeV, but fades as the threshold is raised to 10 TeV. When fully deployed, neutrino observatories of the current generation will have instrumented areas  $A \approx 0.02 \text{ km}^2$ . Although they should register a handful of AGN neutrinos, it will be difficult to distinguish them from the atmospheric background. The energy dependence of the upward-going muon rate will be an important discriminant for separating atmospheric and extraterrestrial sources.

The GRB-WB flux yields a small number of upward-going muon events per year in a  $0.1\text{-km}^2$  detector. To pick these out from the background, it will be essential to correlate them in time and position with gamma-ray bursts. The TD-SLSC flux appears unobservable in a  $0.1\text{-km}^2$  detector.

The ratio of the “nearly horizontal” rate ( $60^\circ < \theta < 90^\circ$ ) to the full upward rate characterizes the attenuation of the incident neutrino flux in the Earth. The energy dependence of the neutrino interaction length shown in Figures 6 and 7 is reflected in the angular dependence of the shadow factor, for given neutrino energy: the greater the neutrino energy, the more the incident neutrino flux is attenuated in its passage through the Earth. We recall that at  $\theta = 60^\circ$ , the column depth is about 20% of the vertical column depth [12]. The ATM and AGN-M95 fluxes fall rapidly with neutrino energy, so rates are dominated by neutrino energies near the muon energy threshold, and attenuation is not severe for  $E_\mu^{\text{min}} = 1 \text{ TeV}$ . For these model fluxes, the upper half of the  $2\pi$  solid angle for upward events contributes between 52% and 58% of the total number of upward-going events. The other model fluxes decrease more slowly with neutrino energy. Accordingly, the effect of shadowing on the angular distribution is more pronounced. For the AGN-SS91 and AGN-M95 fluxes, the “nearly horizontal” solid angle contributes 76% and 87% of the total. The relatively stiff GRB-WB flux also entails significant shadowing: 67% of the events come from the  $1\pi$  solid angle just below the horizon.

The importance of shadowing increases as the muon energy threshold is raised. For  $E_\mu^{\text{min}} = 10 \text{ TeV}$ , between 59% and 89% of the upward rate comes from the upper half of the upward solid angle.

If we raise the muon energy threshold to 100 TeV, the atmospheric neutrino background is essentially eliminated. At the same time, the projected signal rates, shown in Table V for a detector with  $A = 0.1 \text{ km}^2$ , reflect the influence of shadowing in the Earth in two ways. First, the angular distributions favor shallow angles still more strongly. Between 77% and 94% of the extraterrestrial neutrino signal comes from the “nearly horizontal” wedge. Second, the shadow factor  $S(E_\nu)$  drops rapidly above 100 TeV. It is equal to 0.64, 0.34, 0.16, 0.071 for  $E_\nu = 100 \text{ TeV}$ , 1 PeV, 10 PeV, and 100 PeV. Even so, the AGN-SS91 and AGN-P96 upward rates should be observable in a detector with an effective area of  $A = 0.1 \text{ km}^2$ .

The penalty of shadowing overcomes the advantages of looking at upward-going muons as the muon-energy threshold is raised. For very high thresholds, it will be necessary to observe downward-going muons produced by interactions within the instrumented volume. We show in Table VI the annual downward event rates for  $\nu_\mu N$  and  $\bar{\nu}_\mu N$  charged-current interactions in a  $1\text{-km}^3$  volume of water. The rates are encouraging, provided that downward-going events can be observed efficiently.

We discussed the effect of different choices for the parton distribution functions in GQRS96 for energy thresholds of 1 and 10 TeV. We concluded that the upward muon event rate is insensitive to the choice of modern (post-HERA) parton distribution. We have

evaluated the upward muon event rates for  $E_\mu^{\min} = 100$  TeV with the MRS D-' [63] and CTEQ3-DLA [64] parton distributions. The event rates are essentially equal to those shown in Table V.

We indicated in Section II C that all standard parton distribution functions yield very similar cross sections up to  $E_\nu \approx 10^7$  GeV, so only with a muon threshold  $E_\mu^{\min} \gtrsim 10^7$  GeV might one distinguish between parton distribution functions. The angular distribution of the upward muons is a measure of attenuation as a function of column depth, and thus of the cross section. We show in Figure 10 the differential shadow factor  $(1/2\pi) dS/d\cos\theta$  for three neutrino energies and for three sets of parton distributions. At  $E_\nu = 10^3$  GeV, there is no appreciable shadowing at any angle. By  $E_\nu = 10^6$  GeV,  $S(E_\nu) \approx 0.3$ , and the nearly vertical (upward-going) events are depleted in comparison to nearly horizontal events. However, the angular distribution of events will be quite similar for our nominal set of parton distributions (CTEQ4-DIS) and for the CTEQ3-DLA and MRS-D-' distributions. At still higher energies, events will be observed only near the horizon. The angular distribution is steepest for the MRS-D-' distributions, which yield the largest  $\nu N$  cross sections, and shallowest for the CTEQ3-DLA distributions, which yield the smallest  $\nu N$  cross sections. Given the low rates we anticipate for  $E_\nu \gtrsim 10^8$  GeV, a discriminating measurement would demand a prohibitively large instrumented volume.

### C. Neutrino-electron scattering

Observations of electron neutrino interactions at higher energies and large target volumes may yield insights into the ultrahigh energy neutrino flux and the high energy  $\nu N$  cross section. Generically, the  $\nu_e + \bar{\nu}_e$  flux from the  $\pi \rightarrow \mu \rightarrow e$  decay chain is one-half the  $\nu_\mu + \bar{\nu}_\mu$  flux. For the rate estimates presented here, we use the fluxes of Figure 9 multiplied by 0.5. As a cautionary note, we call attention to the contention of Rachen and Meszaros [65] that muon cooling within astrophysical sources may reduce the UHE  $\nu_\mu + \bar{\nu}_\mu$  flux by a factor of two and effectively eliminate the UHE  $\nu_e + \bar{\nu}_e$  flux. In this subsection, we shall first evaluate rates for resonant  $W$  production. Then we consider the possibility of observing nearly horizontal air showers induced by neutrino interactions in the atmosphere.

Resonant  $\bar{\nu}_e e \rightarrow W^-$  production occurs for  $E_{\bar{\nu}} \simeq 6.3$  PeV. In an effective volume  $V_{\text{eff}}$ , the contained event rate is

$$\text{Rate} = \frac{10}{18} N_A V_{\text{eff}} \int_{(M_W - 2\Gamma_W)^2/2m}^{(M_W + 2\Gamma_W)^2/2m} dE_{\bar{\nu}_e} \sigma_{\bar{\nu}_e e}(E_{\bar{\nu}_e}) \frac{dN_{\bar{\nu}_e}}{dE_{\bar{\nu}_e}}. \quad (3.7)$$

Downward resonant  $\bar{\nu}_e e \rightarrow W^-$  rates are shown in Table VII for an effective volume of  $1 \text{ km}^3$ . To assess potential backgrounds to the detection of  $\bar{\nu}_e e \rightarrow W^- \rightarrow \mu \bar{\nu}_\mu$  and  $\bar{\nu}_e e \rightarrow W^- \rightarrow$  hadrons, we also show the downward (and upward)  $(\nu_\mu, \bar{\nu}_\mu)N$  charged-current and neutral-current events that occur for  $E_\nu > 3$  PeV. The  $\nu_e N$  downward and upward interaction rates and the  $\bar{\nu}_e N$  downward interaction rates may be obtained from the  $(\nu_\mu, \bar{\nu}_\mu)N$  rates by scaling the incident fluxes. The  $\bar{\nu}_e N$  upward interaction rates are reduced by the short  $\bar{\nu}_e e$  interaction length near resonance. All of these backgrounds to the identification of  $\bar{\nu}_e e \rightarrow W^- \rightarrow \bar{\nu}_\mu \mu$  or hadrons are themselves evidence for extraterrestrial neutrinos. We conclude, as in GQRS96, that resonant  $W^-$  production will be difficult to extract from

the neutrino-nucleon interaction background. The short  $\bar{\nu}_e$  interaction length at resonance (*cf.* Figure 8) means that the flux of electron antineutrinos is extinguished for neutrinos traversing the Earth.

Let us now take up the observability of neutrino interactions in the atmosphere. A neutrino normally incident on a surface detector passes through a column of density of 1 033 cmwe, while a neutrino arriving along the horizon encounters a column of about 36 000 cmwe. Both amounts of matter are orders of magnitude smaller than the neutrino interaction lengths summarized in Figures 6–8, so the atmosphere is essentially transparent to neutrinos.

However, the horizontal path length low in the atmosphere is not tiny compared with the depth available for the production of contained events in a water or ice Čerenkov detector [66], so it is worth asking what capabilities a large-area air-shower array might have for the study of UHE neutrino interactions. The proposed Pierre Auger Cosmic Ray Observatory [33], which would consist of an array of water Čerenkov tanks dispersed over a large land area, is designed to detect showers of particles produced in the atmosphere. Proton- and photon-induced showers are typically produced high in the atmosphere. Nearly horizontal events with shower maxima near the surface array are more likely to arise from neutrino interactions than from  $p$ -Air or  $\gamma$ -Air collisions [67].

The acceptance  $\mathcal{A}$  of the Auger ground array, which has dimensions of volume times solid angle, has been evaluated by several authors [34,68,69]. We adopt the Billoir’s estimate [34], as shown in Figure 11, to compute the event rate

$$\text{Rate} = N_A \rho_{\text{air}} \int_{E_{\text{th}}}^{E^{\text{max}}} dE_{\text{sh}} \int_0^1 dy \frac{dN_\nu}{dE_\nu} \frac{d\sigma_{\nu N}}{dy}(E_\nu, y) \mathcal{A}(E_{\text{sh}}) . \quad (3.8)$$

The values of  $E^{\text{max}}$  are the same as for our calculation of upward muon rates in §III B. For  $(\nu_e + \bar{\nu}_e)N$  charged-current interactions, we take the shower energy to be the sum of hadronic and electromagnetic energies,  $E_{\text{sh}} = E_\nu$ . For  $(\nu_\mu + \bar{\nu}_\mu)N$  charged-current interactions and for neutral-current interactions, we take the shower energy to be the hadronic energy,  $E_{\text{sh}} = yE_\nu$ . The resulting event rates, calculated using our canonical CTEQ4–DIS parton distributions, are shown in Table VIII for  $(\nu_e + \bar{\nu}_e)N$  neutral-current interactions and for  $(\nu_\mu + \bar{\nu}_\mu)N$  charged-current interactions, for two shower thresholds. The  $(\nu_\mu + \bar{\nu}_\mu)N$  neutral-current rates are twice those shown for the  $(\nu_e + \bar{\nu}_e)N$  case. In Table IX we show our evaluation of the  $(\nu_e + \bar{\nu}_e)N$  charged-current rates for three different sets of parton distributions.

The  $(\nu_e + \bar{\nu}_e)N$  neutral-current event rates are typically less than 15% of the corresponding charged-current rates, reflecting a combination of smaller cross sections and a falling flux. The  $(\nu_\mu + \bar{\nu}_\mu)N$  charged-current rates are a factor of  $\sim 4$  larger than the  $(\nu_e + \bar{\nu}_e)N$  neutral-current rates, because of the larger flux and larger cross section. The inelasticity parameters  $\langle y \rangle$  are approximately equal for neutral-current and charged-current interactions.

The largest rates for neutrino-induced horizontal air showers arise from  $(\nu_e + \bar{\nu}_e)N$  charged-current interactions, for which  $E_{\text{sh}} \approx E_\nu$ . In one year, a few to tens of horizontal  $(\nu_e + \bar{\nu}_e)N \rightarrow e^\mp + \text{anything}$  events may be observed in the Auger detectors, assuming the modern estimates of AGN neutrino fluxes. The AGN-SS91, GRB-WB, TD-SLSC, and TD-WMB16 fluxes yield fractions of an event per year, while the TD-WMB12 flux yields an event or two.

Given the high thresholds that must be set for detection, the expected event rates are dependent on the choice of parton distribution functions. The  $D_-'$  rates are approximately a factor of two larger than the CTEQ3-DLA rates. If the absolute normalization and energy behavior of the AGN fluxes could be established in underground experiments at lower energies, the Auger experiment might suggest distinctions among the various high-energy extrapolations of the cross sections.

#### IV. SUMMARY AND OUTLOOK

We have presented new calculations of the cross sections for neutrino-nucleon charged-current and neutral-current interactions. The new cross sections are at most 25% smaller than those of GQRS96, with the deviation largest at the highest energy considered here,  $10^{21}$  eV. By varying the extrapolations of the small- $x$  behavior of the parton distribution functions, we find that the uncertainty in the  $\nu N$  cross section is at most a factor of  $2^{\pm 1}$  at the highest energies. All modern sets of parton distribution functions give comparable cross sections for energies up to  $10^{16}$  eV.

We have estimated event rates for several energy thresholds and detection methods, using a variety of models for the neutrino fluxes from AGNs, gamma-ray bursters, topological defects, and cosmic-ray interactions in the atmosphere. In  $\nu_\mu N \rightarrow \mu X$  interactions, requiring a muon energy above 10 TeV reduces the atmospheric background enough to permit the observation of upward-going muons for the AGN-SS91 and AGN-P96 fluxes. These models yield tens to hundreds of events per year for detectors of  $0.1 \text{ km}^2$  effective area. The GRB-WB flux emerges at a higher threshold, but suffers from a small event rate.

Event rates for downward muons above 100 TeV from neutrinos are substantial in  $1 \text{ km}^3$ , except for the TD models. Resonant  $W$  boson production will be difficult to distinguish from the  $\nu N$  interaction background. For the Pierre Auger Cosmic Ray Observatory, the most promising rates arise from  $(\nu_e, \bar{\nu}_e)N$  charged-current interactions in the AGN-M95 and AGN-P96 models. By combining measurements of the upward-going muon rate at lower energies with air-shower studies at the highest energies, it may be possible to distinguish among alternative high-energy extrapolations of the  $\nu N$  cross section.

The origins of the highest energy cosmic rays are not well understood, but cosmic rays should be accompanied by very high energy neutrinos in all models. The absolute normalization and energy dependence of the fluxes vary from model to model. Neutrino telescopes ultimately will probe extraterrestrial accelerator sources. We expect that detectors with effective areas on the order of  $0.1 \text{ km}^2$  will yield significant clues to aid in our understanding of physics to the  $10^{20}$ -eV energy scale.

#### ACKNOWLEDGMENTS

RG is grateful for the hospitality of the Department of Physics at the University of Arizona and of the Fermilab Theoretical Physics Department. Fermilab is operated by Universities Research Association, Inc., under contract DE-AC02-76CHO3000 with the United States Department of Energy. CQ thanks the Department of Physics at Princeton University for warm hospitality. MHR acknowledges the hospitality of the CERN Theory Division. The

research of MHR at the University of Iowa is supported in part by National Science Foundation Grant PHY 95-07688. The research of IS at the University of Arizona is supported in part by the United States Department of Energy under contracts DE-FG02-85ER40213 and DE-FG03-93ER40792. CQ, MHR, and IS acknowledge the hospitality of the Aspen Center for Physics.



## REFERENCES

- [1] Y. Totsuka, Rep. Prog. Phys. **55**, 377 (1992).
- [2] T. K. Gaisser, F. Halzen, and T. Stanev, Phys. Rep. **258**, 173 (1995).
- [3] J. N. Bahcall, *et al.*, Nature (London) **375**, 29 (1995).
- [4] S. Barwick, F. Halzen, and P. B. Price, Int. J. Mod. Phys. **A11**, 3393 (1996) (electronic archive: astro-ph/9512079).
- [5] D. W. McKay and J. P. Ralston, Phys. Lett. **167B**, 103 (1986).
- [6] C. Quigg, M. H. Reno, and T. P. Walker, Phys. Rev. Lett. **57**, 774 (1986).
- [7] M. H. Reno and C. Quigg, Phys. Rev. **D37**, 657 (1988).
- [8] A. V. Butkevich, A. B. Kařdalov, P. I. Krastev, A. V. Leonov-Vendrovski, and I. M. Zheleznykh, Z. Phys. **C39**, 241 (1988).
- [9] George M. Frichter, Douglas W. McKay, and John P. Ralston, Phys. Rev. Lett. **74**, 1508 (1995).
- [10] G. Parente and E. Zas, “The High Energy Neutrino–Nucleon Cross Section from Recent HERA Parton Densities,” Contribution EPS 0127 to the International Europhysics Conference on High Energy Physics (HEP 95), Brussels.
- [11] A. V. Butkevich, *et al.*, “Prospects for Radio Wave and Acoustic Detection of Ultra and Super High Energy Cosmic Neutrinos (Cross Sections, Signals, Thresholds),” Contribution EPS 0523 to the International Europhysics Conference on High Energy Physics (HEP 95), Brussels.
- [12] R. Gandhi, C. Quigg, M. H. Reno, and I. Sarcevic, Astropart. Phys. **5**, 81 (1996).
- [13] G. Hill, Astropart. Phys. **6**, 215 (1997).
- [14] K. Hirata, *et al.* (KAMIOKANDE Collaboration), Phys. Rev. Lett. **58**, 1490 (1987); R. M. Bionta, *et al.* (IMB Collaboration), *ibid.* **58**, 1494 (1987).
- [15] K. Hirata, *et al.* (KAMIOKANDE Collaboration), Phys. Rev. **D44**, 2241 (1991).
- [16] K. Inoue, “Solar Neutrinos at Super-Kamiokande,” talk given at the the 5th International Workshop on Topics in Astroparticle and Underground Physics, Gran Sasso, Italy, September 1997, available at <http://www-sk.icrr.u-tokyo.ac.jp/doc/sk/pub/esp crc2.ps.gz>.
- [17] R. Becker-Szendy, *et al.* (IMB Collaboration), Phys. Rev. **D46**, 3720 (1992); and “Neutrino Measurements with the IMB Detector,” in *Neutrino 94*, Proceedings of the Sixteenth International Conference on Neutrino Physics and Astrophysics, edited by A. Dar, G. Eilam, and M. Gronau Nucl. Phys. B (Proc. Supp.) **38**, 331 (1995).
- [18] K. S. Hirata, *et al.* (KAMIOKANDE Collaboration), Phys. Lett. **B280**, 146 (1992).
- [19] K. Daum, *et al.* (Frėjus Collaboration), Z. Phys. **C66**, 417 (1995). This paper contains extensive references to other modern experiments. See also F. Ronga, “High Energy Neutrinos in the MACRO Experiment,” in *Neutrino Telescopes*, Proceedings of the Fifth International Workshop, Venice, 2–4 March 1993, edited by M. Baldo Ceolin, (University of Padua, Padua, 1993), p. 285.
- [20] W. Rhode, *et al.* (Frėjus Collaboration), Astropart. Phys. **4**, 217 (1996). This paper contains extensive comparisons with models of the very-high-energy neutrino flux.
- [21] W. W. M. Allison, *et al.* (Soudan-2 Collaboration), Phys. Lett. **B391**, 491 (1997).
- [22] E. Kearns, “Experimental Measurements of Atmospheric Neutrinos,” presented at TAUP97, the Fifth International Workshop on Topics in Astroparticle and Underground Physics (electronic archive: astro-ph/9803007).

- [23] Y. Fukuda, *et al.* (Super-Kamiokande Collaboration), “Measurement of a small atmospheric  $\nu_\mu/\nu_e$  ratio” (electronic archive: astro-ph/9803006).
- [24] Y. Fukuda, *et al.* (Super-Kamiokande Collaboration), “Study of the atmospheric neutrino flux in the multi-GeV energy range” (electronic archive: hep-ex/9805006).
- [25] For a survey of detectors for neutrino astronomy, see J. G. Learned, *Phil. Trans. Roy. Soc. London A* **346**, 99 (1994). The prototype water Čerenkov detectors are the underground KAMIOKANDE and IMB detectors cited above. A comparison of detection techniques appears in P. B. Price, *Astropart. Phys.* **5**, 43 (1996).
- [26] Many important ideas arose in planning for the Deep Underwater Muon and Neutrino Detector described by V. Z. Peterson, in *Currents in Astrophysics and Cosmology: Papers in Honor of Maurice M. Shapiro*, edited by G. G. Fazio and R. Silberberg (Cambridge University Press, Cambridge, 1994), p. 169; and by P. K. F. Grieder, in *NESTOR*, Third NESTOR International Workshop, 19–21 October 1993, edited by L. K. Resvanis (Athens University Press, Athens, 1994), p. 168. See also R. J. Wilkes, “DUMAND and AMANDA: High-Energy Neutrino Astrophysics,” in *Particle Physics, Astrophysics, and Cosmology*, Proceedings of 22nd Annual SLAC Summer Institute on Particle Physics, edited by L. DePorcel and J. Chan (SLAC, Stanford, CA, 1996), p. 301 (electronic archive: astro-ph/9412019).
- [27] Y. Suzuki, “Kamiokande and Super-Kamiokande,” talk given at the International School of Nuclear Physics (19th course) Neutrinos in Astro, Particle and Nuclear Physics, Erice, Italy, September 1997, available at <http://www-sk.icrr.u-tokyo.ac.jp/doc/sk/pub/erice.ps.gz>.
- [28] The Baikal Neutrino Telescope is described by L. Kuzmichev, “The Baikal Neutrino Project: Status Report,” presented at the 26th International Cosmic Ray Conference, Durban, South Africa, 1997, available at <http://www.ifh.de/baikal/publications/icrc97/status/stat97.ps.gz>.
- [29] A neutrino particle astrophysics underwater laboratory in the Mediterranean is described by L. K. Resvanis, in *Neutrino Telescopes*, Proceedings of the Fifth International Workshop, Venice, 2–4 March 1993, edited by M. Baldo Ceolin, (University of Padua, Padua, 1993), p. 321; L. K. Resvanis, in *NESTOR*, Third NESTOR International Workshop, 19–21 October 1993, edited by L. K. Resvanis (Athens University Press, Athens, 1994), p. 1. E. G. Anassontzis, *et al.* (NESTOR Collaboration), “Status of NESTOR, a deep Sea Neutrino Telescope in the Mediterranean,” presented at the 16th International Workshop on Weak Interactions and Neutrinos (WIN97), Durham; available at <http://www.roma1.infn.it/nestor/win97/win97.ps>. B. Monteleoni, “Neutrino Astronomy and the NESTOR Project,” presented to the ROPAC2 meeting, Manchester, 17 April 1998, available at <http://www.hep.man.ac.uk/iop98/bianca-monteleoni.ps>.
- [30] F. Blanc, *et al.* (ANTARES Collaboration), “ANTARES: Towards a Large Scale High Energy Cosmic Neutrino Undersea Detector,” CPPM-97-02, DAPNIA-97-03, IFIC-97-35, OUNP-97-06 (electronic archive: astro-ph/9707136); available at <http://antares.in2p3.fr/antares/>.
- [31] The Antarctic Muon and Neutrino Detector Array is described by F. Halzen, “The AMANDA Neutrino Telescope: Science Prospects and Performance at First Light,” (electronic archive: astro-ph/9707289).
- [32] Prospects for radio detection of UHE neutrinos are described by G. M.

- Frichter, J. P. Ralston, and D. W. McKay, Phys. Rev. D**53**, 1684 (1996), and by A. L. Provorov and I. M. Zheleznykh, Astropart. Phys. **4**, 55 (1995). For information about the Radio Ice Cerenkov Experiment (RICE), see <http://kuhep4.phsx.ukans.edu/~iceman/index.html>. The RAdio Neutrino Detection project (RAND) is presented at <http://spectrum.lbl.gov/www/rand/rand.html>.
- [33] For a brief introduction, see C. Pryke, “Auger: What, Why, and How,” Pierre Auger project note GAP-98-006, available at [http://www-td-auger.fnal.gov:82/GAP98/GAP\\_98\\_006.ps](http://www-td-auger.fnal.gov:82/GAP98/GAP_98_006.ps). The Design Report is available at [http://www-td-auger.fnal.gov:82/DesignReport/DR\\_page.html](http://www-td-auger.fnal.gov:82/DesignReport/DR_page.html).
- [34] Pierre Billoir, “Estimation of the acceptance of the Auger ground detector to quasi-horizontal showers induced deeply in the atmosphere,” Pierre Auger project note GAP-97-049, available at [http://www-td-auger.fnal.gov:82/GAP97/GAP\\_97\\_049.ps](http://www-td-auger.fnal.gov:82/GAP97/GAP_97_049.ps).
- [35] Information about OWL is available at <http://lheawww.gsfc.nasa.gov/docs/gamcosray/hecr/owl.html>. For a study of upward-going neutrino-induced showers in the atmosphere, see G. Domokos and S. Kovesi-Domokos, “Observation of Ultrahigh Energy Neutrino Interactions by Orbiting Detectors,” JHU-TIPAC-98004 (electronic archive: hep-ph/9805221).
- [36] A preliminary account of this work appears in C. Quigg, “Neutrino Interaction Cross Sections,” FERMILAB-CONF-97/158-T, presented at the Workshop on High-Energy Cosmic Neutrinos, Marseille, 2-3 June 1997.
- [37] H. Lai, *et al.* (CTEQ Collaboration), Phys. Rev. D**51**, 4763 (1995).
- [38] H. L. Lai, *et al.* (CTEQ Collaboration), Phys. Rev. D**55**, 1280 (1997).
- [39] See G. Altarelli, R. K. Ellis, and G. Martinelli, Nucl. Phys. **B143**, 521 (1978).
- [40] R. M. Barnett, Phys. Rev. D**14**, 70 (1976).
- [41] G. Peter Lepage, J. Comput. Phys. **27**, 192 (1978); Cornell University Report CLNS-80/447 (unpublished).
- [42] M. Carena, D. Choudhury, S. Lola, and C. Quigg, “Manifestations of  $R$ -Parity Violation in Ultrahigh-Energy Neutrino Interactions,” FERMILAB-PUB-98/088-T (electronic archive: hep-ph/9804380), to appear in Phys. Rev. D.
- [43] W. Hollik, “Review: Status of the Standard Model,” KA-TP-22-1997, presented at the International Workshop on Quantum Effects in the Minimal Supersymmetric Standard Model, Barcelona, 9-13 September 1997 (electronic archive: hep-ph/9711492), finds  $\sin^2 \theta_W = 0.2236 \pm 0.0041$ .
- [44] F. Abe, *et al.* (CDF Collaboration), Phys. Rev. Lett. **77**, 438 (1996).
- [45] For a study of leptoquark production in ultrahigh-energy neutrino interactions, see M. A. Doncheski and R. W. Robinett, Phys. Rev. D**56**, 7412 (1997); R. W. Robinett, Phys. Rev. D**37**, 84 (1988).
- [46] J. Bordes, *et al.*, Astropart. Phys. **8**, 135 (1998); see also “Post-GZK Air Showers, FCNC, Strongly Interacting Neutrinos, and Duality,” RAL-TR-97-067 (electronic archive: hep-ph/9711438).
- [47] G. Burdman, F. Halzen, and R. Gandhi, Phys. Lett. **B417**, 107 (1998).
- [48] R. J. Protheroe, “High-Energy Neutrinos from Blazars” (electronic archive: astro-ph/9607165) in *Accretion Phenomena and Related Outflows, IAU Colloquium 163*, Volume 121 of the ASP Conference Series, ed. D. T. Wickramasinghe, G. V. Bicknell, and L. Ferrario (Astronomical Society of the Pacific, San Francisco, 1997).

- [49] K. Mannheim, *Astropart. Phys.* **3**, 295 (1995).
- [50] E. Waxman and J. Bahcall, *Phys. Rev. Lett.* **78**, 2292 (1997).
- [51] G. Sigl, S. Lee, D. N. Schramm and P. Coppi, *Phys. Lett.* **B392**, 129 (1997).
- [52] U. F. Wichoski, J. H. MacGibbon, and R. H. Brandenberger, “High Energy Neutrinos, Photons and Cosmic Rays from Non-Scaling Cosmic Strings,” BROWN-HET-1115 (electronic archive: hep-ph/9805419).
- [53] For a recent compilation of muon fluxes as a function of depth, see M. Aglietta, *et al.* (LVD Collaboration), “Muon ‘Depth-Intensity’ Relation Measured by LVD Underground Experiment and Cosmic-Ray Muon Spectrum at Sea Level” (electronic archive: hep-ex/9806001). The depth-vertical-intensity relation is summarized by  $I_\mu(d) = 2.15 \times 10^4 \text{ km}^{-2} \text{ s}^{-1} \text{ sr}^{-1} \lambda^{-1.93} e^{-\lambda}$ , with  $\lambda \equiv d/(1.155 \text{ kmwe})$ .
- [54] To estimate these fluxes, we use the incident flux at the Earth’s surface given in Eqn. (29) of GQRS96 and the Lipari-Stanev range formula of Ref. [55].
- [55] P. Lipari and T. Stanev, *Phys. Rev.* **D44**, 3543 (1991).
- [56] F. W. Stecker, C. Done, M. H. Salamon, and P. Sommers, *Phys. Rev. Lett.* **66**, 2697 (1991); *ibid.* **69**, 2738E (1992). Revised estimates of the neutrino flux appear in F. W. Stecker and M. H. Salamon, “High Energy Neutrinos from Quasars,” *Space Science Reviews* **75**, 341 (1996) (electronic archive: astro-ph/9501064), where it is assumed that all the observed AGN x-ray luminosity arises from hadronic interactions. We have scaled this flux by a factor of 0.3.
- [57] J. R. Klein and A. K. Mann, “Prototype Detector for Ultrahigh Energy Neutrino Detection” (electronic archive: astro-ph/9806152).
- [58] L. V. Volkova, *Yad. Fiz.* **31**, 1510 (1980) [English transl.: *Sov. J. Nucl. Phys.* **31**, 784 (1980)]. The angle-average fluxes are given in Tables 2 and 3.
- [59] Other simulations of the atmospheric neutrino fluxes are in good agreement with the Volkova calculation in the range of interest to us: T. K. Gaisser, T. Stanev, and G. Barr, *Phys. Rev.* **D38**, 85 (1988); G. Barr, T. K. Gaisser, and T. Stanev, *Phys. Rev.* **D39**, 3532 (1989); V. Agrawal, T. K. Gaisser, P. Lipari, and T. Stanev, *Phys. Rev.* **D53**, 1314 (1996); A. Butkevich, L. G. Dedenko, and I. M. Zheleznyh, *Yad. Fiz.* **50**, 142 (1989) [English transl.: *Sov. J. Nucl. Phys.* **50**, 90 (1989)]; K. Mitsui, Y. Minorikawa, and H. Komori, *Nuovo Cim.* **9C**, 995 (1986); P. Lipari, *Astropart. Phys.* **1**, 195 (1993). For a comparison with data, see Figure 10 of Reference [19].
- [60] L. Pasquali, M. H. Reno, and I. Sarcevic, “Lepton fluxes from atmospheric charm” (electronic archive: hep-ph/9806428). We use their central values to compute the “charm” entries in Tables III – VI.
- [61] Y. Fukuda, *et al.* (Super-Kamiokande Collaboration), “Evidence for oscillation of atmospheric neutrinos,” (electronic archive: hep-ex/9807003).
- [62] See Ref. [12] for the details of the Earth model used in this calculation. Parameters come from Adam Dziewonski, Earth Structure, Global, in: *The Encyclopedia of Solid Earth Geophysics*, David E. James, ed. (Van Nostrand Reinhold, New York, 1989) p. 331.
- [63] A. D. Martin, R. G. Roberts and W. J. Stirling, *Phys. Lett.* **B306**, 145 (1993).
- [64] See Ref. [12] for a discussion of the double-log-approximation (DLA) as applied to the small- $x$  behavior of the parton distribution functions.
- [65] J. P. Rachen and P. Meszaros, “Photohadronic neutrinos from transients in astrophysical

- sources" (electronic archive: astro-ph/9802280).
- [66] See Figure 16 of GQRS96, Ref. [12].
  - [67] J. J. Blanco-Pillado, R. A. Vázquez and E. Zas, *Phys. Rev. Lett.* **78**, 3614 (1997).
  - [68] Gonzalo Parente and Enrique Zas, "Neutrino induced events in the Pierre Auger detector," presented at 7th International Workshop on Neutrino Telescopes, Venice, Italy, 27 Feb – 1 Mar 1996 (electronic archive: astro-ph/9606091)
  - [69] K. S. Capelle, J.W. Cronin, G. Parente, and E. Zas, "On the detection of ultrahigh-energy neutrinos with the Auger observatory," *Astropart. Phys.* **8**, 321 (1998) (electronic archive: astro-ph/9801313).

TABLES

TABLE I. Charged-current and neutral-current cross sections and their sum for  $\nu N$  interactions according to the CTEQ4-DIS distributions.

$E_\nu$ [GeV]	$\sigma_{CC}$ [cm <sup>2</sup> ]	$\sigma_{NC}$ [cm <sup>2</sup> ]	$\sigma_{tot}$ [cm <sup>2</sup> ]
$1.0 \times 10^1$	$0.7988 \times 10^{-37}$	$0.2492 \times 10^{-37}$	$0.1048 \times 10^{-36}$
$2.5 \times 10^1$	$0.1932 \times 10^{-36}$	$0.6033 \times 10^{-37}$	$0.2535 \times 10^{-36}$
$6.0 \times 10^1$	$0.4450 \times 10^{-36}$	$0.1391 \times 10^{-36}$	$0.5841 \times 10^{-36}$
$1.0 \times 10^2$	$0.7221 \times 10^{-36}$	$0.2261 \times 10^{-36}$	$0.9482 \times 10^{-36}$
$2.5 \times 10^2$	$0.1728 \times 10^{-35}$	$0.5430 \times 10^{-36}$	$0.2271 \times 10^{-35}$
$6.0 \times 10^2$	$0.3964 \times 10^{-35}$	$0.1255 \times 10^{-35}$	$0.5219 \times 10^{-35}$
$1.0 \times 10^3$	$0.6399 \times 10^{-35}$	$0.2039 \times 10^{-35}$	$0.8438 \times 10^{-35}$
$2.5 \times 10^3$	$0.1472 \times 10^{-34}$	$0.4781 \times 10^{-35}$	$0.1950 \times 10^{-34}$
$6.0 \times 10^3$	$0.3096 \times 10^{-34}$	$0.1035 \times 10^{-34}$	$0.4131 \times 10^{-34}$
$1.0 \times 10^4$	$0.4617 \times 10^{-34}$	$0.1575 \times 10^{-34}$	$0.6192 \times 10^{-34}$
$2.5 \times 10^4$	$0.8824 \times 10^{-34}$	$0.3139 \times 10^{-34}$	$0.1196 \times 10^{-33}$
$6.0 \times 10^4$	$0.1514 \times 10^{-33}$	$0.5615 \times 10^{-34}$	$0.2076 \times 10^{-33}$
$1.0 \times 10^5$	$0.2022 \times 10^{-33}$	$0.7667 \times 10^{-34}$	$0.2789 \times 10^{-33}$
$2.5 \times 10^5$	$0.3255 \times 10^{-33}$	$0.1280 \times 10^{-33}$	$0.4535 \times 10^{-33}$
$6.0 \times 10^5$	$0.4985 \times 10^{-33}$	$0.2017 \times 10^{-33}$	$0.7002 \times 10^{-33}$
$1.0 \times 10^6$	$0.6342 \times 10^{-33}$	$0.2600 \times 10^{-33}$	$0.8942 \times 10^{-33}$
$2.5 \times 10^6$	$0.9601 \times 10^{-33}$	$0.4018 \times 10^{-33}$	$0.1362 \times 10^{-32}$
$6.0 \times 10^6$	$0.1412 \times 10^{-32}$	$0.6001 \times 10^{-33}$	$0.2012 \times 10^{-32}$
$1.0 \times 10^7$	$0.1749 \times 10^{-32}$	$0.7482 \times 10^{-33}$	$0.2497 \times 10^{-32}$
$2.5 \times 10^7$	$0.2554 \times 10^{-32}$	$0.1104 \times 10^{-32}$	$0.3658 \times 10^{-32}$
$6.0 \times 10^7$	$0.3630 \times 10^{-32}$	$0.1581 \times 10^{-32}$	$0.5211 \times 10^{-32}$
$1.0 \times 10^8$	$0.4436 \times 10^{-32}$	$0.1939 \times 10^{-32}$	$0.6375 \times 10^{-32}$
$2.5 \times 10^8$	$0.6283 \times 10^{-32}$	$0.2763 \times 10^{-32}$	$0.9046 \times 10^{-32}$
$6.0 \times 10^8$	$0.8699 \times 10^{-32}$	$0.3837 \times 10^{-32}$	$0.1254 \times 10^{-31}$
$1.0 \times 10^9$	$0.1049 \times 10^{-31}$	$0.4641 \times 10^{-32}$	$0.1513 \times 10^{-31}$
$2.5 \times 10^9$	$0.1466 \times 10^{-31}$	$0.6490 \times 10^{-32}$	$0.2115 \times 10^{-31}$
$6.0 \times 10^9$	$0.2010 \times 10^{-31}$	$0.8931 \times 10^{-32}$	$0.2903 \times 10^{-31}$
$1.0 \times 10^{10}$	$0.2379 \times 10^{-31}$	$0.1066 \times 10^{-31}$	$0.3445 \times 10^{-31}$
$2.5 \times 10^{10}$	$0.3289 \times 10^{-31}$	$0.1465 \times 10^{-31}$	$0.4754 \times 10^{-31}$
$6.0 \times 10^{10}$	$0.4427 \times 10^{-31}$	$0.1995 \times 10^{-31}$	$0.6422 \times 10^{-31}$
$1.0 \times 10^{11}$	$0.5357 \times 10^{-31}$	$0.2377 \times 10^{-31}$	$0.7734 \times 10^{-31}$
$2.5 \times 10^{11}$	$0.7320 \times 10^{-31}$	$0.3247 \times 10^{-31}$	$0.1057 \times 10^{-30}$
$6.0 \times 10^{11}$	$0.9927 \times 10^{-31}$	$0.4377 \times 10^{-31}$	$0.1430 \times 10^{-30}$
$1.0 \times 10^{12}$	$0.1179 \times 10^{-30}$	$0.5196 \times 10^{-31}$	$0.1699 \times 10^{-30}$

TABLE II. Charged-current and neutral-current cross sections and their sum for  $\bar{\nu}N$  interactions according to the CTEQ4-DIS distributions.

$E_\nu$ [GeV]	$\sigma_{\text{CC}}$ [cm <sup>2</sup> ]	$\sigma_{\text{NC}}$ [cm <sup>2</sup> ]	$\sigma_{\text{tot}}$ [cm <sup>2</sup> ]
$1.0 \times 10^1$	$0.3936 \times 10^{-37}$	$0.1381 \times 10^{-37}$	$0.5317 \times 10^{-37}$
$2.5 \times 10^1$	$0.9726 \times 10^{-37}$	$0.3403 \times 10^{-37}$	$0.1313 \times 10^{-36}$
$6.0 \times 10^1$	$0.2287 \times 10^{-36}$	$0.7982 \times 10^{-37}$	$0.3085 \times 10^{-36}$
$1.0 \times 10^2$	$0.3747 \times 10^{-36}$	$0.1307 \times 10^{-36}$	$0.5054 \times 10^{-36}$
$2.5 \times 10^2$	$0.9154 \times 10^{-36}$	$0.3193 \times 10^{-36}$	$0.1235 \times 10^{-35}$
$6.0 \times 10^2$	$0.2153 \times 10^{-35}$	$0.7531 \times 10^{-36}$	$0.2906 \times 10^{-35}$
$1.0 \times 10^3$	$0.3542 \times 10^{-35}$	$0.1243 \times 10^{-35}$	$0.4785 \times 10^{-35}$
$2.5 \times 10^3$	$0.8548 \times 10^{-35}$	$0.3026 \times 10^{-35}$	$0.1157 \times 10^{-34}$
$6.0 \times 10^3$	$0.1922 \times 10^{-34}$	$0.6896 \times 10^{-35}$	$0.2612 \times 10^{-34}$
$1.0 \times 10^4$	$0.3008 \times 10^{-34}$	$0.1091 \times 10^{-34}$	$0.4099 \times 10^{-34}$
$2.5 \times 10^4$	$0.6355 \times 10^{-34}$	$0.2358 \times 10^{-34}$	$0.8713 \times 10^{-34}$
$6.0 \times 10^4$	$0.1199 \times 10^{-33}$	$0.4570 \times 10^{-34}$	$0.1656 \times 10^{-33}$
$1.0 \times 10^5$	$0.1683 \times 10^{-33}$	$0.6515 \times 10^{-34}$	$0.2334 \times 10^{-33}$
$2.5 \times 10^5$	$0.2909 \times 10^{-33}$	$0.1158 \times 10^{-33}$	$0.4067 \times 10^{-33}$
$6.0 \times 10^5$	$0.4667 \times 10^{-33}$	$0.1901 \times 10^{-33}$	$0.6568 \times 10^{-33}$
$1.0 \times 10^6$	$0.6051 \times 10^{-33}$	$0.2493 \times 10^{-33}$	$0.8544 \times 10^{-33}$
$2.5 \times 10^6$	$0.9365 \times 10^{-33}$	$0.3929 \times 10^{-33}$	$0.1329 \times 10^{-32}$
$6.0 \times 10^6$	$0.1393 \times 10^{-32}$	$0.5930 \times 10^{-33}$	$0.1986 \times 10^{-32}$
$1.0 \times 10^7$	$0.1734 \times 10^{-32}$	$0.7423 \times 10^{-33}$	$0.2476 \times 10^{-32}$
$2.5 \times 10^7$	$0.2542 \times 10^{-32}$	$0.1100 \times 10^{-32}$	$0.3642 \times 10^{-32}$
$6.0 \times 10^7$	$0.3622 \times 10^{-32}$	$0.1578 \times 10^{-32}$	$0.5200 \times 10^{-32}$
$1.0 \times 10^8$	$0.4430 \times 10^{-32}$	$0.1937 \times 10^{-32}$	$0.6367 \times 10^{-32}$
$2.5 \times 10^8$	$0.6278 \times 10^{-32}$	$0.2762 \times 10^{-32}$	$0.9040 \times 10^{-32}$
$6.0 \times 10^8$	$0.8696 \times 10^{-32}$	$0.3836 \times 10^{-32}$	$0.1253 \times 10^{-31}$
$1.0 \times 10^9$	$0.1050 \times 10^{-31}$	$0.4641 \times 10^{-32}$	$0.1514 \times 10^{-31}$
$2.5 \times 10^9$	$0.1464 \times 10^{-31}$	$0.6489 \times 10^{-32}$	$0.2113 \times 10^{-31}$
$6.0 \times 10^9$	$0.2011 \times 10^{-31}$	$0.8931 \times 10^{-32}$	$0.2904 \times 10^{-31}$
$1.0 \times 10^{10}$	$0.2406 \times 10^{-31}$	$0.1066 \times 10^{-31}$	$0.3472 \times 10^{-31}$
$2.5 \times 10^{10}$	$0.3286 \times 10^{-31}$	$0.1465 \times 10^{-31}$	$0.4751 \times 10^{-31}$
$6.0 \times 10^{10}$	$0.4481 \times 10^{-31}$	$0.1995 \times 10^{-31}$	$0.6476 \times 10^{-31}$
$1.0 \times 10^{11}$	$0.5335 \times 10^{-31}$	$0.2377 \times 10^{-31}$	$0.7712 \times 10^{-31}$
$2.5 \times 10^{11}$	$0.7306 \times 10^{-31}$	$0.3247 \times 10^{-31}$	$0.1055 \times 10^{-30}$
$6.0 \times 10^{11}$	$0.9854 \times 10^{-31}$	$0.4377 \times 10^{-31}$	$0.1423 \times 10^{-30}$
$1.0 \times 10^{12}$	$0.1165 \times 10^{-30}$	$0.5195 \times 10^{-31}$	$0.1685 \times 10^{-30}$

TABLE III. Upward  $\mu^+ + \mu^-$  event rates per year arising from  $\nu_\mu N$  and  $\bar{\nu}_\mu N$  interactions in rock, for a detector with effective area  $A = 0.1 \text{ km}^2$  and muon energy threshold  $E_\mu^{\text{min}} = 1 \text{ TeV}$ . The rates are shown integrated over all angles below the horizon and restricted to “nearly horizontal” nadir angles  $60^\circ < \theta < 90^\circ$ .

Flux	nadir angular acceptance	
	$0^\circ < \theta < 90^\circ$	$60^\circ < \theta < 90^\circ$
ATM [58]	1100	570
ATM [58] + charm [60]	1100	570
AGN-SS91 [56]	500	380
AGN-M95 ( $p\gamma$ ) [49]	31	18
AGN-P96 ( $p\gamma$ ) [48]	45	39
GRB-WB [50]	12	8.1
TD-SLSC [51]	0.005	0.0046
TD-WMB12 [52]	0.50	0.39
TD-WMB16 [52]	0.00050	0.00039

TABLE IV. Upward  $\mu^+ + \mu^-$  event rates per year arising from  $\nu_\mu N$  and  $\bar{\nu}_\mu N$  interactions in rock, for a detector with effective area  $A = 0.1 \text{ km}^2$  and muon energy threshold  $E_\mu^{\text{min}} = 10 \text{ TeV}$ . The rates are shown integrated over all angles below the horizon and restricted to “nearly horizontal” nadir angles  $60^\circ < \theta < 90^\circ$ .

Flux	nadir angular acceptance	
	$0^\circ < \theta < 90^\circ$	$60^\circ < \theta < 90^\circ$
ATM [58]	17	10
ATM [58] + charm [60]	19	11
AGN-SS91 [56]	270	210
AGN-M95 ( $p\gamma$ ) [49]	5.7	4.3
AGN-P96 ( $p\gamma$ ) [48]	28	25
GRB-WB [50]	5.4	4.0



TABLE V. Upward  $\mu^+ + \mu^-$  event rates per year arising from  $\nu_\mu N$  and  $\bar{\nu}_\mu N$  interactions in rock, for a detector with effective area  $A = 0.1 \text{ km}^2$  and muon energy threshold  $E_\mu^{\text{min}} = 100 \text{ TeV}$ . The rates are shown integrated over all angles below the horizon and restricted to “nearly horizontal” nadir angles  $60^\circ < \theta < 90^\circ$ .

Flux	nadir angular acceptance	
	$0^\circ < \theta < 90^\circ$	$60^\circ < \theta < 90^\circ$
ATM [58]	0.13	0.09
ATM [58] + charm [60]	0.21	0.16
AGN-SS91 [56]	85	73
AGN-M95 ( $p\gamma$ ) [49]	1.6	1.5
AGN-P96 ( $p\gamma$ ) [48]	13	12
GRB-WB [50]	1.2	1.0

TABLE VI. Downward  $\mu^+ + \mu^-$  events per year arising from  $\nu_\mu N$  and  $\bar{\nu}_\mu N$  interactions in  $1 \text{ km}^3$  of water.

Flux	Muon-energy threshold, $E_\mu^{\text{min}}$		
	100 TeV	1 PeV	3 PeV
ATM [58]	0.85	0.0054	0.00047
ATM [58] + charm [60]	2.6	0.050	0.0076
AGN-SS91 [56]	520	120	42
AGN-M95 ( $p\gamma$ ) [49]	16	11	8.7
AGN-P96 ( $p\gamma$ ) [48]	100	50	31
GRB-WB [50]	7.7	1.9	0.93
TD-SLSC [51]	0.037	0.032	0.029
TD-WMB12 [52]	1.1	0.74	0.58
TD-WMB16 [52]	0.00087	0.00050	0.00035

TABLE VII. Downward resonant  $\bar{\nu}_e e \rightarrow W^-$  events per steradian per year for a detector with effective volume  $V_{\text{eff}} = 1 \text{ km}^3$ . Also shown are the downward (upward) potential background rates from  $\nu_\mu N$  and  $\bar{\nu}_\mu N$  interactions induced by neutrinos with  $E_\nu > 3 \text{ PeV}$ .

Flux	$\bar{\nu}_e e \rightarrow \bar{\nu}_\mu \mu$	$\bar{\nu}_e e \rightarrow \text{hadrons}$	$(\nu_\mu, \bar{\nu}_\mu)N$ CC		$(\nu_\mu, \bar{\nu}_\mu)N$ NC	
AGN-SS91 [56]	6	41	29	(5.2)	13	(2.3)
AGN-M95 ( $p\gamma$ ) [49]	0.1	0.6	2.3	(0.21)	1.1	(0.095)
AGN-P96 ( $p\gamma$ ) [48]	1.2	7.8	12	(1.6)	5.2	(0.69)
GRB-WB [50]	0.06	0.4	0.43	(0.065)	0.19	(0.029)
TD-SLSC [51]	0.001	0.0074	0.0059	(0.00031)	0.0028	(0.00014)

TABLE VIII. Annual neutral-current  $(\nu_e, \bar{\nu}_e)N$  and charged-current  $(\nu_\mu, \bar{\nu}_\mu)N$  event rates for the Pierre Auger Cosmic Ray Observatory.

Flux	$E_{\text{sh}} > 10^8 \text{ GeV}$		$E_{\text{sh}} > 10^9 \text{ GeV}$	
	$(\nu_e, \bar{\nu}_e)N$ NC	$(\nu_\mu, \bar{\nu}_\mu)N$ CC	$(\nu_e, \bar{\nu}_e)N$ NC	$(\nu_\mu, \bar{\nu}_\mu)N$ CC
AGN-SS91 [56]	0.0045	0.019	0.000006	0.000024
AGN-M95 ( $p\gamma$ ) [49]	0.65	2.7	0.26	1.1
AGN-P96 ( $p\gamma$ ) [48]	0.74	3.1	0.13	0.53
GRB-WB [50]	0.038	0.16	0.020	0.085
TD-SLSC [51]	0.013	0.052	0.010	0.042
TD-WMB12 [52]	0.15	0.59	0.11	0.44
TD-WMB16 [52]	0.000026	0.00011	0.000011	0.000046

TABLE IX. Annual event rates in the Pierre Auger Cosmic Ray Observatory for horizontal air showers induced by  $(\nu_e, \bar{\nu}_e)N$  charged-current interactions.

Flux	Parton distributions	$E_{\text{sh}} > 10^8 \text{ GeV}$	$E_{\text{sh}} > 10^9 \text{ GeV}$
AGN-SS91 [56]	CTEQ4-DIS	0.15	0.00026
	CTEQ3-DLA	0.13	0.00022
	D <sub>2</sub> '	0.23	0.00051
AGN-M95 ( $p\gamma$ ) [49]	CTEQ4-DIS	6.1	3.3
	CTEQ3-DLA	5.3	2.8
	D <sub>2</sub> '	12	7.5
AGN-P96 ( $p\gamma$ ) [48]	CTEQ4-DIS	8.9	2.6
	CTEQ3-DLA	7.9	2.2
	D <sub>2</sub> '	16	5.4
GRB-WB [50]	CTEQ4-DIS	0.31	0.18
	CTEQ3-DLA	0.27	0.16
	D <sub>2</sub> '	0.67	0.45
TD-SLSC [51]	CTEQ4-DIS	0.068	0.061
	CTEQ3-DLA	0.056	0.051
	D <sub>2</sub> '	0.18	0.17
TD-WMB12 [52]	CTEQ4-DIS	0.85	0.71
	CTEQ3-DLA	0.72	0.60
	D <sub>2</sub> '	2.1	1.9
TD-WMB16 [52]	CTEQ4-DIS	0.00024	0.00014
	CTEQ3-DLA	0.00021	0.00012
	D <sub>2</sub> '	0.00049	0.00032

## FIGURES

## FIGURES

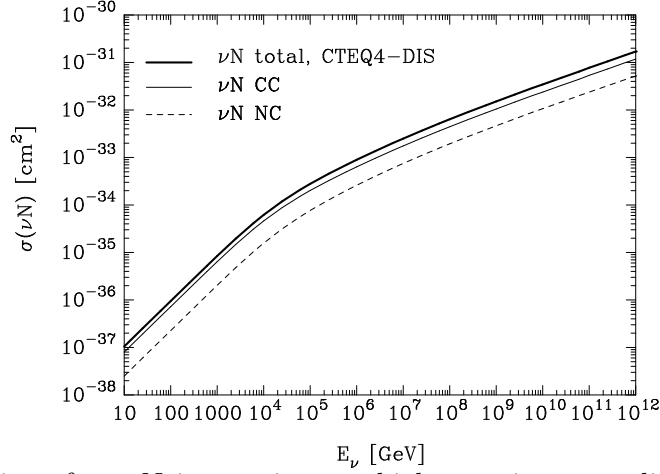


FIG. 1. Cross sections for  $\nu_\ell N$  interactions at high energies, according to the CTEQ4-DIS parton distributions: dashed line,  $\sigma(\nu_\ell N \rightarrow \nu_\ell + \text{anything})$ ; thin line,  $\sigma(\nu_\ell N \rightarrow \ell^- + \text{anything})$ ; thick line, total (charged-current plus neutral-current) cross section.

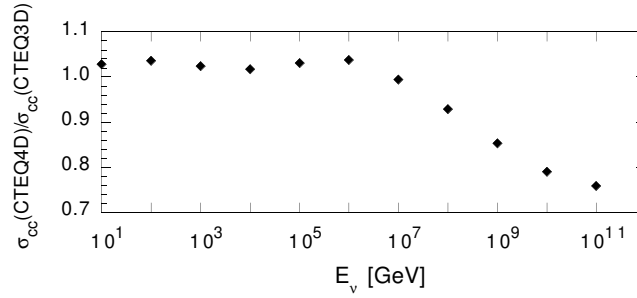


FIG. 2. Ratio of the charged-current cross section shown in Figure 1, calculated using the CTEQ4-DIS parton distributions, to the charged-current cross section of Ref. [12] calculated using the CTEQ3-DIS parton distributions.

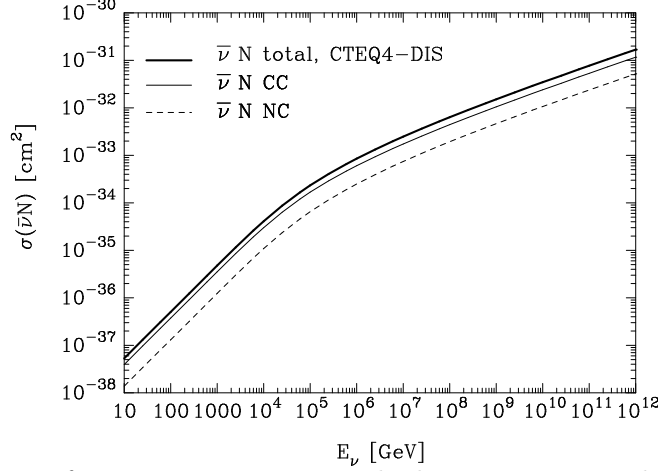


FIG. 3. Cross sections for  $\bar{\nu}_\ell N$  interactions at high energies, according to the CTEQ4-DIS parton distributions: dashed line,  $\sigma(\bar{\nu}_\ell N \rightarrow \bar{\nu}_\ell + \text{anything})$ ; thin line,  $\sigma(\bar{\nu}_\ell N \rightarrow \ell^+ + \text{anything})$ ; thick line, total (charged-current plus neutral-current) cross section.

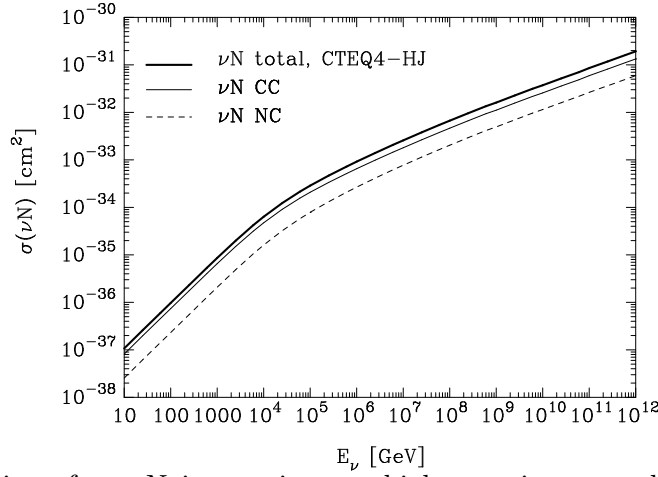


FIG. 4. Cross sections for  $\nu_\ell N$  interactions at high energies, according to the CTEQ4-HJ parton distributions: dashed line,  $\sigma(\nu_\ell N \rightarrow \nu_\ell + \text{anything})$ ; thin line,  $\sigma(\nu_\ell N \rightarrow \ell^- + \text{anything})$ ; thick line, total (charged-current plus neutral-current) cross section.

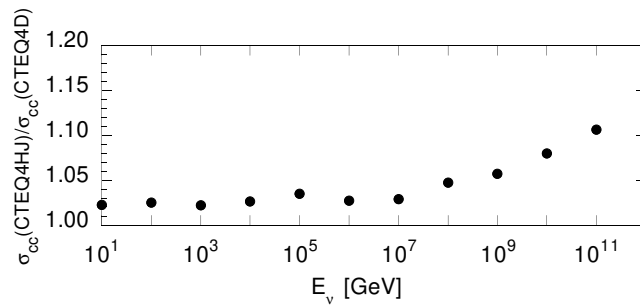


FIG. 5. Ratio of the charged-current cross section shown in Figure 4, calculated using the CTEQ4-HJ parton distributions, to the charged-current cross section of Figure 1 calculated using the CTEQ4-DIS parton distributions.

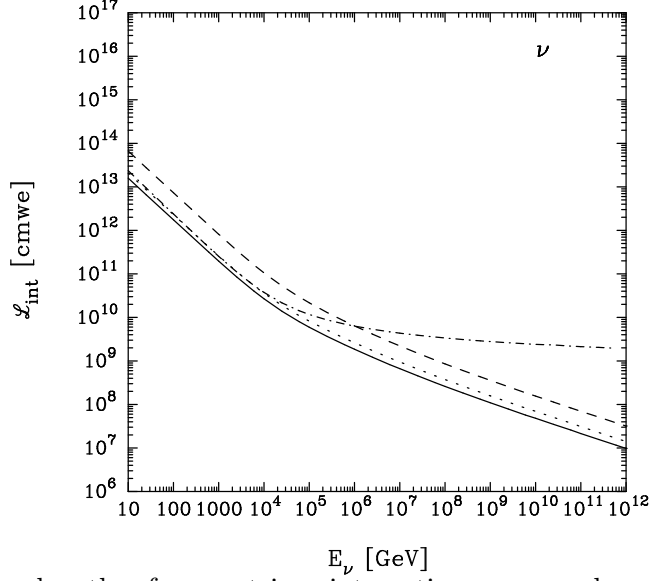


FIG. 6. Interaction lengths for neutrino interactions on nucleon targets: dotted line, charged-current interaction length; dashed line, neutral-current interaction length; solid line, total interaction length, all computed with the CTEQ4–DIS parton distributions. The dot-dashed curve shows the charged-current interaction length based on the EHLQ structure functions with  $Q^2$  held fixed at  $Q_0^2 = 5 \text{ GeV}^2$ .

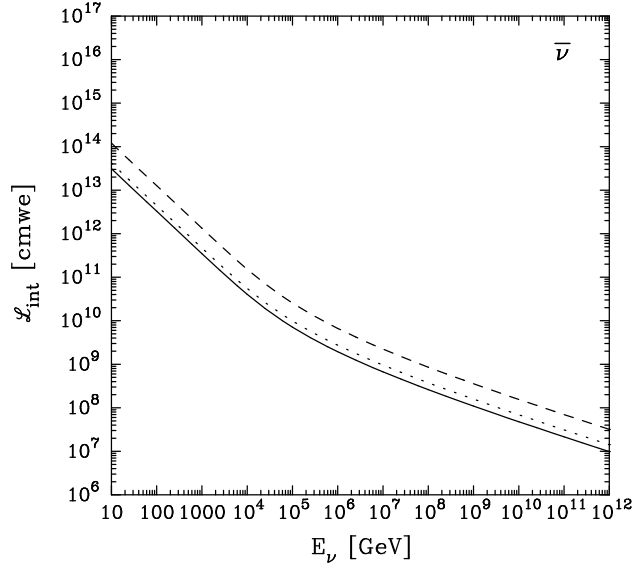


FIG. 7. Interaction lengths for antineutrino interactions on nucleon targets: dotted line, charged-current interaction length; dashed line, neutral-current interaction length; solid line, total interaction length, all computed with the CTEQ4–DIS parton distributions.

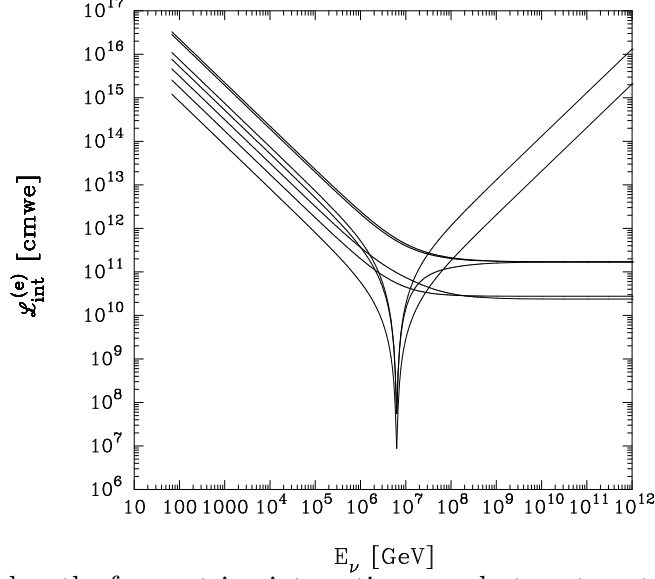


FIG. 8. Interaction lengths for neutrino interactions on electron targets. At low energies, from smallest to largest interaction length, the processes are (i)  $\bar{\nu}_e e \rightarrow$  hadrons, (ii)  $\nu_\mu e \rightarrow \mu \nu_e$ , (iii)  $\nu_e e \rightarrow \nu_e e$ , (iv)  $\bar{\nu}_e e \rightarrow \bar{\nu}_\mu \mu$ , (v)  $\bar{\nu}_e e \rightarrow \bar{\nu}_e e$ , (vi)  $\nu_\mu e \rightarrow \nu_\mu e$ , (vii)  $\bar{\nu}_\mu e \rightarrow \bar{\nu}_\mu e$ . [From Ref. [12]]

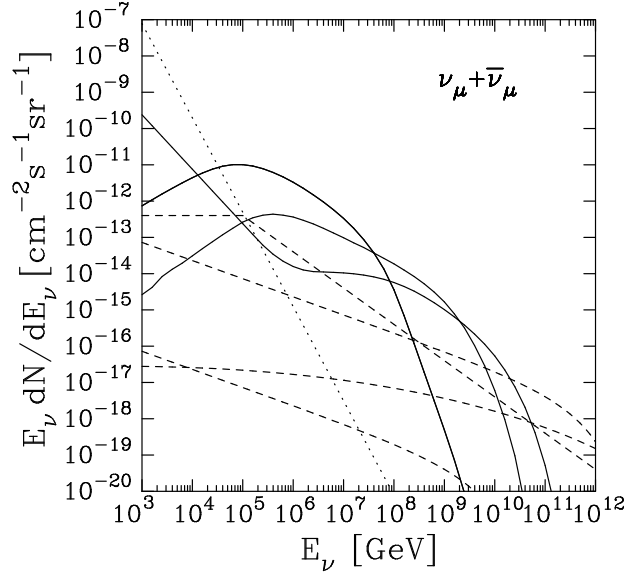


FIG. 9. Muon neutrino plus antineutrino fluxes scaled by neutrino energy at the Earth's surface. Solid lines represent AGN fluxes. In decreasing magnitude at  $E_\nu = 10^3$  GeV, they are AGN-M95, AGN-SS91 scaled by 0.3, and AGN-P96 ( $p\gamma$ ). The dashed lines, in the same order, represent the GRB-WB, TD-WMB12, TD-WMB16, and TD-SLSC fluxes. The dotted line is the angle-averaged atmospheric (ATM) neutrino flux.

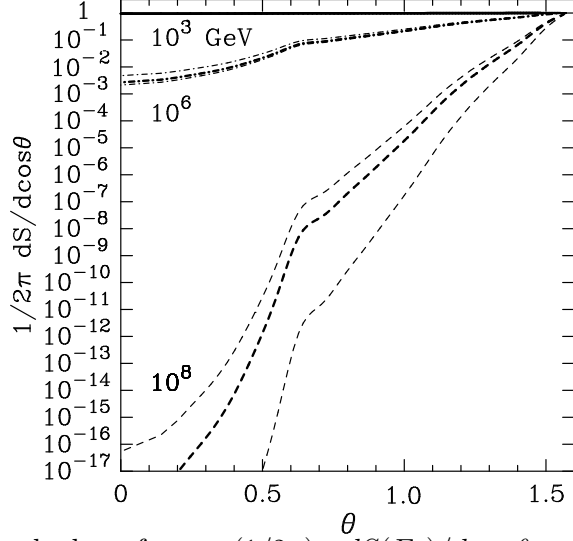


FIG. 10. Differential shadow factor  $(1/2\pi) \frac{dS(E_\nu)}{d\cos\theta}$  versus nadir angle  $\theta$ , for  $E_\nu = 10^3$  GeV (solid line),  $10^6$  GeV (dot-dashed lines), and  $10^8$  GeV (dashed lines). For each neutrino energy, the thick line corresponds to the CTEQ4-DIS parton distributions; the upper and lower satellite lines correspond to the CTEQ3-DLA and MRS-D' parton distributions, respectively.

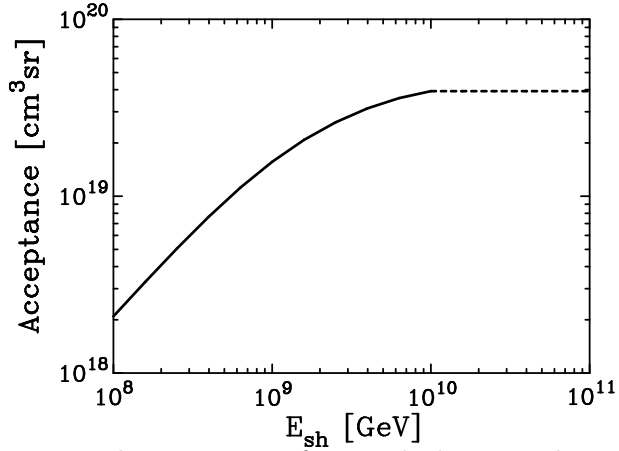


FIG. 11. Acceptance versus shower energy for nearly horizontal air showers in the proposed Pierre Auger Cosmic Ray Observatory. The solid line for  $E_{\text{sh}} \leq 10^{10}$  GeV shows the acceptance evaluated by Billoir [34]; the dashed line is our projection to higher energies.